Available online at www.sciencedirect.com
ScienceDirect
International Journal of Multiphase Flow 33 (2007) 987–1005
International Journal of Multiphase Flow
www.elsevier.com/locate/ijmulflow

Experimental study of turbulence-induced coalescence in aerosols

P. Duru [1], D.L. Koch *, C. Cohen

School of Chemical and Biomolecular Engineering, Cornell University, NY 14853, USA

Received 16 May 2006; received in revised form 28 March 2007

Abstract

In this paper, measurements of the rate of aerosol coalescence in a well characterized turbulent flow are presented. The time dependence of the aerosol droplets' mean radius upon initiation of flow in an oscillating grid generated turbulence chamber is determined using a phase-Doppler method. Together with a measurement of the aerosol number density from a light attenuation probe, the observed rate of change of the aerosol droplets' mean radius can be related to the rate constant for the coalescence of two droplets. The Kolmogorov shear rate, which is the primary parameter in theories predicting coalescence rate, is determined from measurements of the root-mean-square fluctuating velocity and the integral length scale. Our experimental results are compared with theoretical predictions, obtained by solving of the population balance equation. Various expressions are considered for the coalescence rate constant to be used in the population balance equation. First, we considered various combinations of *ideal* coalescence rate constants, i.e. obtained theoretically neglecting particle interactions. Our data are then found to be in good agreement with theoretical predictions that take into account the simultaneous effects of turbulent shear induced and Brownian motion induced coalescence. Second, our results are compared with a theory that considers the effects of turbulent shear and Brownian motion as well as the non-continuum hydrodynamic and van der Waals interparticle interactions. The measured experimental values are generally 50–100% higher than those predicted by this theory. This discrepancy could be explained by the small polydispersity of the aerosol which may result in coalescence induced by differential sedimentation and turbulent acceleration.

Keywords: Coalescence; Coagulation; Aerosol; Experiment; Turbulent flow

1. Introduction

In an aerosol consisting of a dispersion of small droplets, coalescence occurs when Brownian motion, differential sedimentation or fluid flow drive two droplets into contact and the droplets coalesce to form a larger drop. The term coagulation is used to describe the formation of aggregates from solid aerosol particles by the

* Corresponding author. Tel.: +1 607 255 8656; fax: +1 607 255 9166.
E-mail address: dlk15@cornell.edu (D.L. Koch).
[1] Present address: Institut de Mécanique des Fluides de Toulouse, GEMP, Allée Camille Soula, 31400 Toulouse, France.

0301-9322/$ - see front matter © 2007 Elsevier Ltd. All rights reserved.
doi:10.1016/j.ijmultiphaseflow.2007.03.006

same mechanisms. Situations where the fluid flow driving the particle motion is turbulent are found in many industrial processes as well as in natural environments. For instance, in aerosol reactors, submicron aerosol particles formed by combustion coagulate due to Brownian motion and turbulent shear to form fine solid particles (Friedlander, 2000). In atmospheric clouds, where large turbulent intensities are achieved, coalescence induced by turbulence plays an important role in the early stages of the rain droplets' growth (Shaw, 2003).

The rate at which two species of particles, with radii a_i and a_j and number densities n_i and n_j coalesce to form larger particles of radius a_k can be described as

$$-\frac{\mathrm{d}n_i}{\mathrm{d}t} = -\frac{\mathrm{d}n_j}{\mathrm{d}t} = \frac{\mathrm{d}n_k}{\mathrm{d}t} = k_{ij} n_i n_j, \tag{1}$$

where k_{ij} is the coalescence rate constant[2] (Friedlander, 2000). The coalescence rate constant depends not only on the mechanisms driving the relative motion of the particles but also on the hydrodynamic and colloidal interactions that affect the relative motion of the particles as they collide.

The theoretical description of coalescence mechanisms, leading to quantitative predictions for coalescence rate constants is a challenging problem. Early theoretical studies focused on the determination of "ideal" rate constants, which are defined as the rate of coalescence that would occur in the absence of interparticle interactions, if one of the driving forces for coalescence acted in the absence of the other mechanisms. Thus, early results were obtained for coalescence induced by Brownian motion (Smoluchowski, 1916), laminar shear (Smoluchowski, 1917) and differential sedimentation (Findheisen, 1939). Saffman and Turner (1956) were the first to deal with the problem of turbulence-induced coalescence, in the case of aerosol particles much smaller than the Kolmogorov length scale, i.e. the length scale of the smallest turbulent eddies. It ranges from about 1 mm in environmental applications down to 50 μm in high speed industrial flows (Krone, 1978; O'Melia, 1980). The small scales of turbulence, having the largest shear rates, are primarily responsible for coalescence. Saffman and Turner calculated the ideal coalescence rate constant associated with the turbulent shearing motion and found $k_{ij} = 1.3\Gamma(a_i + a_j)^3$, where Γ is the Kolmogorov shear rate, i.e. the shear rate associated with Kolmogorov scale eddies. Saffman and Turner also argued that, for a polydisperse aerosol, there are some collisions driven by the small lags in the particles responses to turbulent accelerations. More recent work underlines the deviations from Saffman and Turner's result for the coalescence rate constant that can be expected when considering large particles. Sundaram and Collins (1997) noted that the deviations can result from two effects, the change in the relative velocity of colliding particles and the change in the probability density for their relative position. Kruis and Kusters (1997) developed a model for the relative velocity of inertial particles. The direct-numerical simulations of Sundaram and Collins (1997), Reade and Collins (2000) and Wang et al. (2000) and the theoretical analysis of Chun et al. (2004) have quantified the increase of the coalescence rate due to the enhanced probability density caused by the preferential concentration of inertial particles.

So far, the theoretical results mentioned are for ideal coalescence rate constants, obtained when neglecting interparticle interactions. More recent studies have shown that the inclusion of continuum hydrodynamic and van der Waals interactions can lead to predicted rates of colloidal coagulation in liquids that agree quantitatively with careful experiments (Brunk et al., 1998a,b). In the case of turbulent-shear induced coalescence, Brunk et al. (1998b) found good agreement between their measurements and their simulation results, when interparticle interactions were taken into account. The coalescence rate constant was written as the product of the ideal coalescence rate constant k^0 and of an efficiency coefficient: $k = \alpha k^0$. Typical values for the efficiency ranged between 0.1 and 0.4 (Brunk et al., 1998a), which highlights the need for incorporating interactions in the coalescence description to obtain quantitative estimates of the coalescence rate constant. Achieving the same level of understanding for aerosol coalescence requires taking account of the non-continuum nature of the hydrodynamic interaction between colliding particles when the interparticle distance becomes comparable with the mean free path of the gas. Following an approach similar to that of Brunk et al. (1998a), Chun and Koch (2005) computed the coalescence rate constant of initially monodisperse aerosol particles in isotropic turbulence, with non-continuum hydrodynamic and van der Waals interactions. Non-

[2] The same formalism is also used in coagulation problems, and k_{ij} is then called the *coagulation* rate constant. Theoretical results mentioned in this paper apply equally to coalescence and coagulation rates.

continuum effects and larger van der Waals forces between aerosol particles (compared to hydrosol particles) lead to larger efficiencies for aerosol coalescence than hydrosol coagulation (Chun and Koch, 2005).

Although extensive experiments have been performed on the Brownian coagulation of aerosols that are small enough to be unaffected by sedimentation (see, for instance, Wagner and Kerker, 1977) and on large sedimenting droplets (see, for instance, Abbott, 1974), the current experimental knowledge of aerosol coalescence due to turbulence is scarce. In particular, there is a dearth of experimental measurements of the coalescence rate constant. Such experiments require a precise characterization of the turbulent flow field. One must also make accurate measurements of the change in the properties of aerosols with sufficiently high concentrations so that the coalescence rate is significant; this is challenging. In addition, one must be concerned about the likelihood that measurements of aerosol coalescence on Earth are influenced by coupled effects of Brownian motion, turbulent shear and acceleration and gravitational settling, making a quantitative comparison with theory difficult. We are aware of only three attempts to measure the coagulation rate constant of solid aerosol particles, in stirred tanks (Langstroth and Gillepsie, 1947; Okuyama et al., 1977) or in a turbulent pipe flow (Okuyama et al., 1978). In these studies, coagulation effects are observed by measuring the decay of the aerosol number density once the turbulent flow is initiated. Since the turbulent flow field was not measured in these experiments, it is necessary to use engineering correlations whose accuracy may be uncertain to interpret the experimental results.

In this paper, we present experimental results concerning the coalescence of aerosols in a turbulent flow. In our experiment, an initially nearly monodisperse aerosol with high particle number density flows continuously through a turbulence chamber where it experiences the turbulent flow field generated by an oscillating grid. The initial drop radius distribution is then modified due to turbulence-induced coalescence and measurement of the aerosol mean radius evolution allows us to determine the coalescence rate constant. The paper is organized as follows. In Section 2, we first describe the experimental setup (Section 2.1). Then, we present the experimental techniques used in our study: laser-Doppler and hot-wire velocimetry on one hand, to characterize the turbulent flow experienced by the particles (see Section 2.2) and phase-Doppler anemometry and a light attenuation technique on the other hand, to characterize the aerosol properties (drop radius distribution and number density), see Section 2.3. The condensation aerosol generator is also presented in Section 2.3. Experimental results concerning the flow characterization in our turbulence chamber are given in Section 3. From these measurements, we can estimate the Kolmogorov shear rate experienced by the aerosol particles. This is an essential parameter when comparisons with theory are considered. In Section 4, we relate the measured aerosol properties to the coalescence rate constant. Then, in Section 5, our experimental results are compared with theoretical predictions and discussed. Conclusions are drawn in Section 6.

2. Experimental techniques

2.1. Experimental apparatus

Aerosol coalescence was studied in the nearly isotropic turbulence produced by an oscillating grid. A sketch of the experimental setup is shown in Fig. 1. The central part of the chamber consisted of a Plexiglas cubic section of size $25 \times 25 \times 25$ cm^3. There was a constant input of aerosol material, injected at the top of a pyramidal section surmounting the central part of the chamber. The aerosol material flowed continuously through the turbulence chamber. At the bottom of the chamber, it was directed to a fume hood using an exhaust pipe. The grid consisted of a commercial plain steel woven wire cloth. The wire diameter was 3.4 mm and the mesh spacing 2.5 cm, leading to a grid solidity of 25%. The grid was positioned in the middle of the chamber and fitted into it with a 1 mm clearance from the walls. The two shafts holding the grid were fixed to a linear motion slider which was connected to a variable speed motor by an eccentric drive system. The grid oscillation amplitude, or stroke, was changed by modifying the eccentricity and its frequency was tuned by varying the motor speed. In this study, the turbulent flow field was characterized for stroke values in the range 6–10 cm and for frequencies in the range 2–5.5 Hz.

It proved useful to be able to remove some aerosol material from the chamber (see Section 2.3.2). A sampling technique was developed for that purpose. The sampler was a tube (1 cm inner diameter) whose entrance could be positioned at different locations in the chamber by passing the tube through several different openings

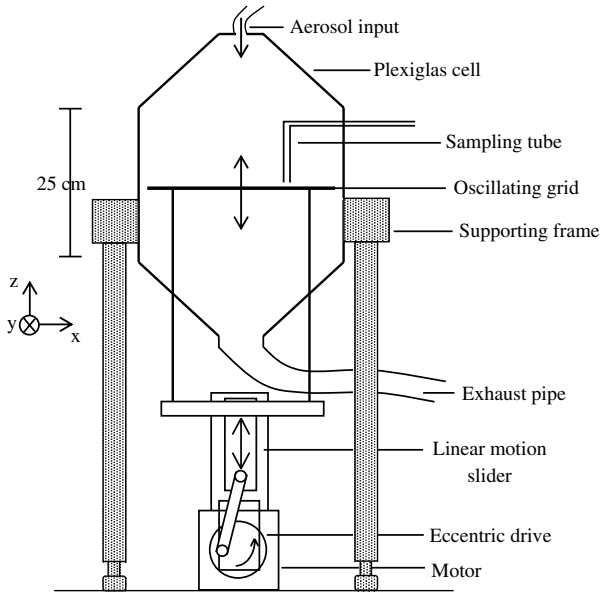

Fig. 1. Sketch of the experimental apparatus.

in the chamber walls. Using a bent tube, it could even be positioned in the grid region (see Fig. 1). A gentle suction was imposed at the tube end located outside the chamber which ensured the smooth removal of some aerosol material from the chamber for further characterization. The sampled aerosol was directed towards the fume hood after analysis. It was verified that, although not isokinetic, the sampling technique did not introduce any bias in the particle radius distribution measured. This was done by changing suction strength or sampling tube length and checking that the measured drop radius distribution remained the same.

2.2. Turbulent flow characterization: laser Doppler velocimetry and hot-wire anemometry

Horizontal (x-direction in Fig. 1) and vertical (z-direction in Fig. 1) velocity fluctuations were measured using a single-component laser-Doppler velocimeter (LDV) operating in the burst-processing mode (a single velocity measurement per Doppler burst). It measured the component of a tracer velocity that was perpendicular to the scattering plane. The scattering plane orientation relative to the chamber could be changed by rotating the transmitting laser unit. The gas flow was seeded with water aerosol droplets produced by a Baxter compressed-air nebulizer. The radius distribution of the water droplets was measured using a Particle Dynamics Analyzer (see Section 2.3.2 for more details). The aerosol number density was typically around 10^4 particles cm^{-3} and the mean radius was kept in the range 2–3 μm with no droplets having a diameter larger than 5 μm. These particles of negligible inertia thus acted as tracers for the turbulent flow. Mean data acquisition rates were between 200 Hz and 800 Hz, depending on the flow seeding and the location of the volume of measurement (higher rates were obtained in flow regions where the turbulent intensity was the largest, see Section 3.1). A transit time weighting was used when calculating the mean and root-mean-square (rms) values of the velocity (Edwards, 1987). The LDV measurement is an Eulerian measurement of the velocity at a given position in the chamber. An integral length scale cannot be obtained directly from this measurement. It was rather calculated using the integral time scale τ based on the temporal autocorrelation function. The integral length scale was taken to be $\tau \times u'$ where u' is the rms velocity at the given location, as in Hannoun et al. (1988) and De Silva and Fernando (1992).

To check the results obtained by LDV, we also performed some measurements using a TSI IFA-300 constant temperature anemometer. A single probe sensor was attached to an arm driven at a constant velocity along a circular path in a horizontal (x–y) plane, allowing a measurement of the horizontal velocity fluctuations, as in Thompson and Turner, 1975. The hot wire anemometer measurements gave the velocity as a

function of position, so an integral length scale could be obtained directly from the area under the horizontal velocity autocorrelation curve.

2.3. Aerosol production and characterization

2.3.1. Aerosol production

Accurate measurement of the coalescence rate requires a highly concentrated aerosol. Indeed, a typical time scale for coalescence to affect the initial aerosol radius distribution is $\tau_c = 1/(k\ n)$, where n is the aerosol number density and k the coalescence rate. The larger the value of n, the more likely it is that the effect of coalescence on the drop radius distribution can be detected during the finite residence time of the aerosol in the chamber and the more likely it is that coalescence will be more significant than wall deposition. Consequently, the device selected to generate the aerosols used in our study was a Condensation Monodisperse Aerosol Generator (TSI, CMAG 3475). The aerosol is generated by controlled heterogeneous condensation. Vaporized aerosol material, Di-Ethyl-Hexyl-Sebacate (DEHS) oil, is recondensed in a controlled manner onto small sodium chloride (NaCl) particles serving as condensation nuclei. This forced condensation allows one to obtain a fair degree of monodispersity. DEHS oil is a low vapor pressure liquid so that the size of the droplets does not vary due to evaporation during the duration of a typical experiment.

In our study, the aerosol number density was varied in the range 1.5×10^5–2×10^6 particles cm^{-3}. The aerosol mean radius a_0 ranged from 1 μm to 2.5 μm. Aerosol drop radius distributions at the output of the aerosol generator were measured using the phase Doppler technique (see Section 2.3.2). Two examples of the radius distributions obtained with this technique are shown in Fig. 2. The aerosol monodispersity was found to be adversely affected by increasing NaCl nuclei concentration. Also, for a given nuclei concentration, radius distributions were broader for smaller particle sizes. In our study requiring highly concentrated aerosol, geometric standard deviations for the aerosol radius distributions were found to range between 1.15 and 1.35 depending on the aerosol mean radius and number density. The aerosol volumetric flow rate at the aerosol generator output was 4 dm^3 per minute. An estimate of the residence time of the aerosol in the 24 dm^3 chamber was then approximately 360 s.

2.3.2. Aerosol radius distribution measurement

The experimental technique used to measure the aerosol radius distribution was phase-Doppler anemometry. The equipment selected was a Particle Dynamic Analyzer (PDA), consisting of a Dantec 58N70 Fiber PDA detection unit and a 58N80 Signal Processor. The measurement principle is based on the analysis of the light scattered by a spherical particle as it moves through a volume of measurement defined by the intersection of two laser beams (for more details on the measurement principle, see for instance Crowe et al., 1998).

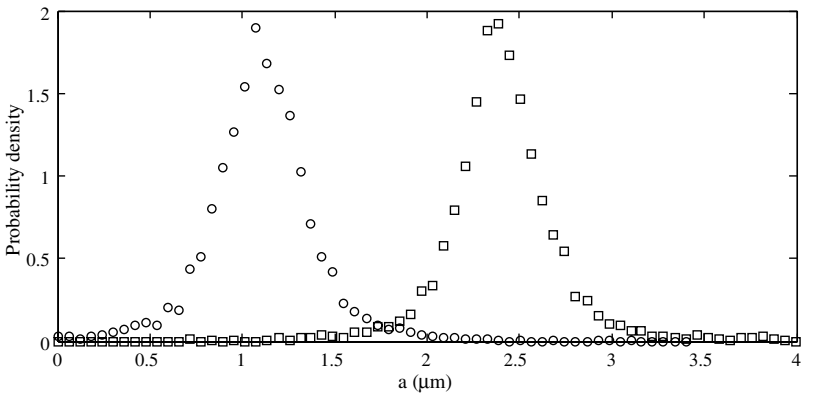

Fig. 2. Two examples of the initial aerosol radius distribution measured at the outlet of the aerosol generator using the phase-Doppler technique. The normalized probability density function is shown as a function of the droplet radius a.

As far as our experiment is concerned, the main advantages of this technique are its very good temporal resolution and accuracy which allow small and rapid changes in aerosol radius distribution to be measured.

In our experiments, a scattering angle of 40° was used, which ensured that first-order refraction was the dominant mode of scattering for DEHS droplets with an index of refraction $n_p = 1.45$. The small aerosol droplets remained spherical. Drop deformation due to gas flow was negligible for the aerosols droplets used in this study, which had a Capillary number $\mathrm{Ca} = \mu_f \Gamma a/\gamma \approx \mathrm{O}(0.01)$, where a is the droplet radius, μ_f is the gas viscosity, γ the droplet superficial tension and Γ the Kolmogorov shear rate (see Section 3).

A PDA unit is a single particle counting device; for the measurement to be correct, there has to be at most one particle in the volume of measurement at any time. As we aimed at measuring the radius distribution of fairly concentrated aerosol, it was important to understand how our results were affected by this constraint. The Dantec 58N80 processor rejects *multi-occurrence* events which lead to electronic signals consisting of two or more superimposed Doppler bursts. Although Edwards and Marx (1992) have shown that differences in the sensitivity of the measurement to particles of different size, can lead to biased results in the particle size distribution obtained from *single occurrence* events, this effect is likely to be small in our study due to the relatively high degree of monodispersity of our aerosol even after coalescence has occurred. To demonstrate this lack of bias, we verified that increasing the sensitivity of the detectors (photo-multiplier tubes), which increases the size of the volume of measurement, decreased the fraction of *single occurrence* events but did not change the measured radius distribution.

In addition, for the PDA system used in the present study, there is a lag between the electrical response of the photo-multiplier and the light input. A built-in calibration system compensates for this effect. We found that the aerosol mean radius measurements performed before and after such a calibration could differ by 4%. This gives an estimate of the uncertainty in the measurement of the drop radius.

2.3.3. Measurement of the aerosol initial number density

A light attenuation technique was used to measure the aerosol initial number density (before the grid is turned on). The extinction of a parallel beam of laser light in the aerosol was measured using an optical fiber probe that could be inserted in the turbulence chamber through openings in one of the side walls. The beam attenuation is described by the Bouguet–Lambert–Beer law:

$$I = I_0 \exp(-l\ nQ_e), \tag{2}$$

where I_0 and I are the light intensity received at the detector respectively without and with scattering particles in between the transmitting and receiving part of the probe (which are separated by a distance l), and Q_e is the extinction efficiency of the aerosol of number density n (van de Hulst, 1981). The aerosol normalized radius distribution $P(a)$ is measured by the PDA system so that the extinction efficiency Q_e of the aerosol can be calculated:

$$Q_e = \int_0^\infty q_e(a)\pi a^2 P(a)\,\mathrm{d}a, \tag{3}$$

where $q_e(a)$ is the scattering efficiency for a particle of radius a, obtained using the Mie theory. The Bouguet–Lambert–Beer's law is valid in the limit of single scattering and a resulting condition for its validity is $l\ nQ_e < 0.15$ (van de Hulst, 1981).

For a given value of l, the attenuation measurement was made the following way. The probe was inserted rapidly though an opening in the chamber wall so that there were no leaks of aerosol material. It was held in the chamber for a few seconds and then removed from the chamber. The acquired signal allowed measurement of the ratio I/I_0. This was repeated 10 times and the attenuation and uncertainty were taken respectively as the mean and standard deviation of the values obtained for I/I_0.

During the course of a coalescence experiment, four attenuation measurements (for $l = 3$, 4, 5, and 6 mm) were performed, to measure the initial aerosol number density n_i. The aerosol radius distribution was measured before and after a measurement at a given l. Slight differences in the size distribution arising from the calibration uncertainty mentioned earlier were taken into account in evaluating the uncertainty in Q_e. The number density was finally obtained as the best fitting slope of the data $\ln(I/I_0)/Q_e$ as a function of l. The uncertainty in the n_i value was typically on the order of 10–20%.

2.4. Experimental procedure

It will be shown in Section 4 that our theoretical description of the experiment relates the coalescence rate constant to the evolution of the mean aerosol radius once the grid is turned on. This measurement was performed in the following manner. Once the aerosol generator had been turned on and set to produce the desired initial particle size distribution, its output was connected to the chamber. In order to reach a steady operation mode, the chamber was allowed to fill for 8 min, a time larger than the aerosol residence time in the chamber. Once this filling stage was completed, a steady state, characterized by the initial number density n_i (then measured as explained above) and aerosol mean radius a_0, had been reached in the chamber. The aerosol mean radius evolution $\langle a\rangle(t)$ was then measured by the PDA system for 5 min. The grid was turned on 30 s after the initiation of the PDA measurement. After each run, the chamber was emptied using a vacuum cleaner, allowed to fill again for 8 min and a new run was started. For each experiment, i.e. for a given initial radius a_0 and turbulence intensity, the measurement of $\langle a\rangle(t)$ was repeated a dozen times. As the aerosol generator settings were not disturbed during an experiment, the number density n_i and the initial aerosol radius distribution were the same at the beginning of each run. All the runs were then averaged and the standard deviation of $\langle a\rangle(t)/a_0$ at a given time divided by the square root of the number of runs was taken as an estimate of the error.

It should be mentioned that in our theoretical description, the turbulence chamber will be treated as an ideal continuous stirred-tank reactor. This assumption is corroborated by our measurements of the turbulent flow in the chamber (see Section 3.2). To test experimentally for the existence of a well mixed region, we measured $\langle a\rangle(t)/a_0$ at different locations in the chamber. It was found to be independent of position when the sampling tube was positioned in various locations within the grid region and up to 3 cm above the top position of the oscillating grid ($z = B/2 + 3$ cm). This result supports the existence of a well-mixed region in the central part of the chamber. Measurements of the aerosol size distribution could then be performed by sampling aerosol particles at any location in this well-mixed region.

3. Characterization of oscillating grid turbulence

Comparison of our experimental results for the coalescence rate constant with theory requires the determination of the Kolmogorov shear rate Γ experienced by the aerosol droplets in the chamber. The inverse of the Kolmogorov shear rate and the Kolmogorov length scale η are the relevant time and length scales for the small scales of turbulence which drive the coalescence of small aerosol drops. Using scaling arguments (see, for instance, Tennekes and Lumley, 1972), Γ and η can be related to the turbulent dissipation rate per unit mass ϵ and the fluid kinematic viscosity ν:

$$\Gamma = (\epsilon/\nu)^{1/2} \quad \text{and} \quad \eta = (\nu^3/\epsilon)^{1/4}. \tag{4}$$

The turbulent dissipation rate can be related to an integral length scale of the turbulent flow, L, and the root-mean-square turbulent velocity fluctuations, u', by the relation:

$$\epsilon \approx K\frac{(u')^3}{L}, \tag{5}$$

where the constant K is usually taken as 0.8 (Townsend, 1976). Combining Eqs. (4) and (5) leads to the following relation for the Kolmogorov shear rate:

$$\Gamma \approx \left[\frac{Ku'^3}{L\nu}\right]^{\frac{1}{2}}. \tag{6}$$

Thus, estimation of the Kolmogorov shear rate requires experimental measurements of u' and L. These measurements were performed in our study and their results are presented in the next subsection (Section 3.1). Then, the estimates of the Kolmogorov shear rate are given in Section 3.2.

Although there are extensive experimental results concerning turbulent flows generated using oscillating grids in water (Thompson and Turner, 1975; Hopfinger and Toly, 1976; E and Hopfinger, 1986; Brumley

and Jirka, 1987), experimental measurements of the flow produced by oscillating grids in air have not been reported previously in the literature, to our knowledge. In water, measurements indicate that the turbulent flow produced is nearly isotropic. The flow is nearly homogeneous in planes parallel to the grid (that is at a given z in our coordinate system, see Fig. 1) and there is a well established scaling law that relates the turbulent velocity fluctuations to the mesh spacing of the grid M, the frequency, f, and stroke, B, of grid oscillation and the distance z from the center of the grid oscillation:

$$u' = cfB^{3/2}M^{1/2}/(z - z_0), \tag{7}$$

where c is a constant of approximately 0.25 (Hopfinger and Toly, 1976; De Silva and Fernando, 1992) and z_0 is the so-called virtual origin. It must be noted that this result applies at sufficiently large distances from the grid, where the measurements were performed. In the same fashion, it has been found that the integral length scale L increases linearly with z away from the grid with the proportionality constant ranging from 0.1 to 0.35 depending on the grid stroke and mesh spacing (Hopfinger and Toly, 1976; E and Hopfinger, 1986; Brumley and Jirka, 1987). However, in our study, knowledge of the turbulent velocity fluctuations and integral length scales is required not only away from the grid but also in the *grid region* (that is the region that the grid traverses). Indeed, the aerosol droplets flow slowly through the chamber and experience the highest level of turbulence when in this grid region. We are aware of only one experimental study of oscillatory grid generated flow in water where results for the grid region were presented (Brunk et al., 1998b).

3.1. Experimental results

We used LDV to measure the temporal velocity fluctuations of the gas both within the grid region, i.e. the region of the chamber where the grid is oscillating, $-B/2 < z < B/2$, and the region above the grid, $z > B/2$. We assumed that the flow is symmetric about $z = 0$ so that it was unnecessary to make measurements below the grid. Details about the processing of our LDV data are given in Appendix I. Typical results concerning the root-mean-square of the horizontal velocity fluctuations, u'_x, are displayed as a function of z in Fig. 3a. Turbulent velocity fluctuations were found to be constant in most of the region of the oscillating grid, that is for $-B/2 + 0.25\text{ cm} < z < +B/2 - 0.25\text{ cm}$, and then decayed away from the grid. A decay law $u'_x \sim (z - z_0)^{-1}$ for $z > z_0$, with $z_0 = B/2 - 0.5$ cm, was found to fit our data away from the grid. This decay law is indicated by the continuous line in Fig. 3a. Both hot-wire anemometry and LDV were used to measure the horizontal velocity fluctuations away from the grid. The values for the horizontal velocity fluctuations obtained with the hot-wire system (filled circles in Fig. 3a) were in good agreement with those obtained by LDV (open circles in Fig. 3a). Similar results were obtained for u'_z as far as the dependence on z is concerned. It was also found that

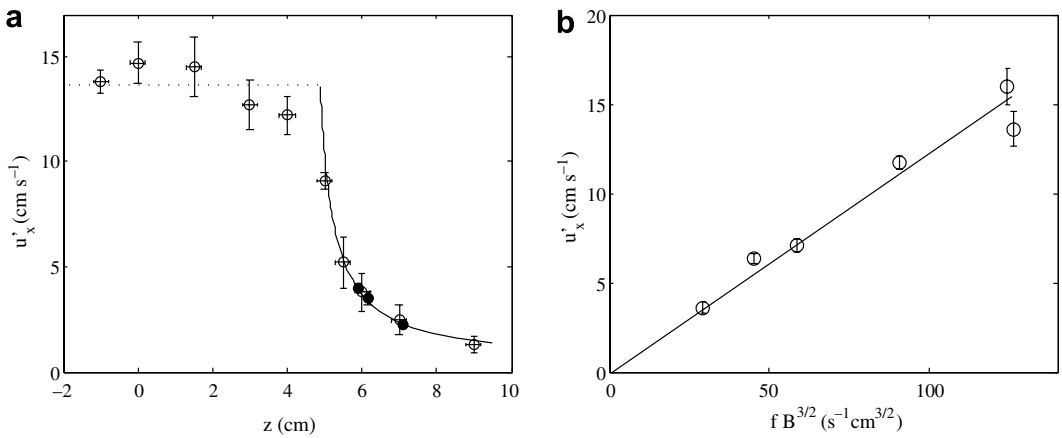

Fig. 3. (a) Horizontal rms velocity fluctuations u'_x as a function of z; open circles: LDV data, filled circles: hot-wire anemometry data. The continuous line is the best fitting decay law, $u'_x \sim (z - z_0)^{-1}$, for $z > z_0$, with $z_0 = B/2 - 0.5$ cm. These results were obtained for a grid stroke $B = 10$ cm and a grid frequency of 4 Hz. (b) Horizontal rms velocity fluctuations u'_x in the grid region plotted as a function of $fB^{3/2}$.

$u'_z \approx 1.25u'_x$ at any position z (for a given stroke and frequency). At a given position z, when comparing results obtained at different grid strokes and frequencies, we found that a scaling law $u' \propto fB^{3/2}$ holds, for data in the grid region (see Fig. 3b) and data in the far field as well.

These results are similar to those obtained previously for oscillatory grid generated flow in water. In particular, Brunk et al. (1998b) observed constant velocity fluctuations in the region traversed by the grid with a rapid decay of the fluctuations beyond this region, in agreement with our results presented in Fig. 3. The slight anisotropy found in our study, $u'_z/u'_x \approx 1.25$, is comparable to the one found by Hopfinger and Toly (1976), Hannoun et al. (1988) and De Silva and Fernando (1992) for oscillating grid turbulence in water, far from the grid. We also observed the same scaling law $u' \propto fB^{3/2}$, as noted in these previous studies. A direct comparison to the scaling of the velocity fluctuations with z in the far field $z \to \infty$ investigated for instance by Hopfinger and Toly (1976) and De Silva and Fernando (1992) cannot be made because our measurements were restricted to regions close to the grid where the turbulence intensity is sufficiently high to drive significant coalescence.

Besides measurements of the turbulent velocity fluctuations, estimation of the Kolmogorov shear rate also requires measurements of the turbulent flow integral length scale L, see Eq. (6). As mentioned in Section 2.2, the integral length scale was taken to be $u' \times \tau$ where u' and τ are respectively the rms velocity and the integral time scale. The integral time scale was obtained from the autocorrelation functions which were computed as the inverse Fourier transform of the velocity fluctuations spectra. In Table 1, L_x and L_z denote the integral length scales obtained from LDV data for the horizontal and vertical velocity fluctuations, respectively. The integral length scales were found to be independent on the grid stroke and frequency. They were constant in the grid region and grew with increasing $|z|$ outside the grid region. We also give in Table 1 the results for the integral length for horizontal velocity fluctuations, L_{HWA}, obtained using the hot-wire probe as explained in Section 2.2. The integral length scales obtained from the hot wire probe were comparable but somewhat larger than those obtained from the LDV measurements. Because we required the integral length over all space and the hot wire measurements were available only outside the grid region, we used the LDV measurements for L_x and L_z to estimate the Kolmogorov shear rate in the following subsection.

3.2. Determination of the spatially averaged Kolmogorov shear rate $\langle \Gamma \rangle$

In our experiment, a *volume average* Kolmogorov shear rate characterized the turbulent shearing experienced by the particles because the grid motion created a turbulent flow and, in the grid region, a temporally oscillating mean flow (see Appendix I) acted to mix the aerosol so that aerosol droplets sampled all positions within the turbulence chamber. Indeed, a homogeneous aerosol is expected if the characteristic time $\tau_c = 1/k\ n$ for coalescence to alter the size distribution is much longer than the mixing time. The characteristic coalescence time was in the range $\mathrm{O}(10^2$–$10^3)$ s in our experiments (see Section 5). The mixing time due to the turbulence can be estimated conservatively as $\tau_m = H^2/u'L$ where H is the size of the mixed region, $u' = \mathrm{O}(10)$ cm s^{-1} is the fluctuating velocity, and $L = \mathrm{O}(0.5)$ cm is the integral length scale. If we consider the grid region $H = 6$–10 cm, we obtain $\tau_m \approx 20$ s. However, in the grid region where most of the turbulent shearing was present, we also expected some mixing to occur due to the oscillatory mean flows (see Appendix I), with a typical mixing time of $\sim B/\langle u_z \rangle$, i.e. a few seconds. This was much shorter than the characteristic coalescence time and we expected the central region of the turbulence chamber to be well-mixed, which was confirmed by our measurements (see Section 2.4).

Table 1
Comparisons of integral length scales

	L_x (mm)	L_z (mm)	L_{HWA} (mm)
Grid region	3 ± 0.3	4.8 ± 0.4	Not measured
$z = B$	4.1 ± 0.3	4.8 ± 0.4	Not measured
$z = B + 0.5$	4 ± 0.3	5 ± 0.5	Not measured
$z = B + 1$	4 ± 1	7 ± 1	6.5 ± 1
$z = B + 2$	6 ± 1	7 ± 2	9 ± 1

Table 2
Values of the spatially averaged Kolmogorov shear rate $\langle \Gamma \rangle$ and of the Kolmogorov length scale η for the different combinations of grid stroke and frequency used in this study

	$\langle \Gamma \rangle$ (s^{-1})	η (μm)	Γ_{mean} (s^{-1})	ϵ ($cm^2\ s^{-3}$)	Re_L
$B = 8$ cm, $f = 5.5$ Hz	92 ± 11	395 ± 30	16 ± 1	1566	49
$B = 10$ cm, $f = 4$ Hz	88 ± 11	403 ± 30	14 ± 1	1433	43
$B = 8$ cm, $f = 4$ Hz	59 ± 9	492 ± 45	11 ± 0.5	644	35
$B = 8$ cm, $f = 2$ Hz	25 ± 3	755 ± 50	5.5 ± 0.5	116	19
$B = 6$ cm, $f = 4$ Hz	24 ± 3	755 ± 50	6.5 ± 0.5	107	18

The values of Γ_{mean} are obtained as explained in Appendix I. The corresponding values of the turbulent dissipation rate $\epsilon = \nu\langle \Gamma \rangle^2$ and of the Reynolds number $Re_L = u'L/\nu$ are also given.

The volume average Kolmogorov shear rate can be obtained using Eq. (6) as:

$$\langle \Gamma \rangle = \frac{1}{2z_{max}} \int_{-z_{max}}^{z_{max}} \left(\frac{Ku'(z)^3}{L(z)\nu} \right)^{1/2} dz = \frac{1}{z_{max}} \times \int_0^{z_{max}} \left(\frac{Ku'(z)^3}{L(z)\nu} \right)^{1/2} dz. \tag{8}$$

In this expression, we assumed homogeneity in planes perpendicular to the grid and reflectional symmetry about the oscillating grid mean position ($z = 0$), and we integrated over the central cubic part of the chamber only ($z_{max} = 12.5$ cm). We took $u' = (2 + \kappa)u'_x/3$, where κ is the anisotropy ratio: $\kappa = u'_z/u'_x = 1.25$. The dependence of u' on z was shown in Fig. 3: u' was taken to be constant in the range $-B/2 + 0.25$ cm $< z < +B/2 - 0.25$ cm and to decay as $C/(z - (B/2 - 0.5))$ for $z > +B/2 - 0.25$ cm, where the constant C is obtained by fitting our data. A piecewise continuous function made of values presented in Table 1 was used for the integral length scale L, with $L = (2L_x + L_z)/3$. When moving away from the grid, the velocity fluctuations decrease and L increases. As a result, it is found that the grid region contributes 80–90% of the value of $\langle \Gamma \rangle$ for the range of grid strokes and frequencies covered in this study. Table 2 shows the value of $\langle \Gamma \rangle$ obtained for the range of B and f values investigated, and the corresponding Kolmogorov length scale $\eta = (\nu/\langle \Gamma \rangle)^{1/2}$. The Kolmogorov length scales in our stirred chamber are much larger than the mean aerosol radius. In Table 2, we also give estimates for the turbulent dissipation rate, the Reynolds number and the shear rates associated with the mean flow, $\Gamma_{mean} \approx 2\langle u_z \rangle / M$, see Appendix I, which are found to be much smaller than $\langle \Gamma \rangle$.

4. Theoretical modeling of the experiment

4.1. Continuous population balance equation

In our experiment, the continuous population balance equation describing the time-dependent change in particle size distribution $p(a, t)$ of the aerosol undergoing coalescence can be written:

$$\frac{\partial p(a,t)}{\partial t} = \frac{p_{in}(a)}{\tau_r} - \frac{p(a,t)}{\tau_l(a)} + \frac{1}{2} \int_0^a K(a', a'') p(a', t) p(a'', t) \frac{a^2\, da'}{(a^3 - a'^3)^{2/3}} - \int_0^\infty K(a', a) p(a', t) p(a, t)\, da', \tag{9}$$

where $K(a, a')$ is the coalescence rate constant and $a'^3 + a''^3 = a^3$. Here, we treated our turbulence chamber as an ideal continuous stirred-tank reactor. Consequently, a source term appears in the population balance, $p_{in}(a)/\tau_r$, which represents the continuous injection of an aerosol stream with radius distribution $p_{in}(a)$ into the chamber (τ_r is the residence time of the gas in the chamber). Also, the effluent aerosol stream and particle losses due to deposition on the chamber walls and grid or sedimentation, are taken into account by the term $-p(a, t)/\tau_l(a)$, so that:

$$\frac{1}{\tau_l(a)} = \frac{1}{\tau_r} + \sum_i \beta_i(a), \tag{10}$$

where each β_i is the loss rate associated with a given particle loss mechanism (sedimentation, Brownian diffusion to the walls, etc.). At the start of the experiment, the aerosol is injected into the chamber with the grid stationary for a sufficient time so that the radius distribution reaches a steady state value $p(a, t = 0) = p(a)$

obtained by the balance of particle injection and particle loss terms in the absence of coalescence: $p(a) = (\tau_l(a)/\tau_r) \times p_{\text{in}}(a)$. The aerosol mean radius at time t is given by:

$$\langle a \rangle(t) = \frac{\int_0^\infty ap(a,t)\,\mathrm{d}a}{\int_0^\infty p(a,t)\,\mathrm{d}a}. \tag{11}$$

4.2. Short time expansion of the continuous population balance equation and evolution of the aerosol mean radius

In the following, we will use the normalized initial radius distribution $P(a) = p(a)/n_i$. We will also take into account the fact that the deposition mechanisms are modified when the grid is started, by making a distinction between $\tau_l^-(a)$ (before initiation of grid motion) and $\tau_l^+(a)$ (after initiation of grid motion). For a given deposition mechanism (for instance Brownian deposition to the walls), the associated β_i can change when the flow field in the chamber becomes turbulent. Also, new deposition mechanisms (namely interception and inertial impaction on the moving grid) are introduced when the grid is started.

Expanding the particle size distribution as a power series in terms of t, the time after the initiation of grid motion:

$$P(a,t) = P(a) + A(a)t + B(a)t^2 + \cdots \tag{12}$$

and substituting the expansion into the population balance equation yields:

$$A(a) = n_i^2 A^*(a) + n_i P(a)\left(\frac{1}{\tau_l^-(a)} - \frac{1}{\tau_l^+(a)}\right), \tag{13}$$

where

$$A^*(a) = \int_0^a \frac{K(a',a'')}{2} P(a')P(a'')\frac{a^2\,\mathrm{d}a'}{(a^3 - a'^3)^{2/3}} - \int_0^\infty K(a,a')P(a')P(a)\,\mathrm{d}a'. \tag{14}$$

The evolution of the mean aerosol radius at short time is then obtained by inserting the short time expansion for $p(a,t)$ in Eq. (11):

$$\langle a \rangle(t) = a_0 + t\left[n_i \int_0^\infty (a-a_0)A^*(a)\,\mathrm{d}a + \int_0^\infty (a-a_0)P(a)\left(\frac{1}{\tau_l^-(a)} - \frac{1}{\tau_l^+(a)}\right)\mathrm{d}a\right] + \mathrm{O}(t^2). \tag{15}$$

In Section 4.2.1, we will argue that, in our experiments, sedimentation is the dominant mechanism for particle losses and that this mechanism is unaffected by the grid motion, so that $\tau_l^-(a) \approx \tau_l^+(a)$. As a result, the early aerosol radius evolution, once the grid is turned on, is primarily due to coalescence and Eq. (15) may be written:

$$\frac{\langle a \rangle(t)}{a_0} = 1 + \frac{tn_i}{a_0}\int_0^\infty (a-a_0)A^*(a)\,\mathrm{d}a = 1 + tn_i J, \tag{16}$$

where J is an integral function of $P(a)$, a_0 and $K(a,a')$:

$$J = \frac{1}{a_0}\int_0^\infty (a-a_0)A^*(a)\,\mathrm{d}a. \tag{17}$$

4.2.1. Particle loss in the experiment

Many theoretical and experimental works have aimed to predict and/or measure wall deposition rates as a function of particle radius in a rectangular vessel where the flow field is turbulent (see early calculations by Corner and Pendlebury, 1951; and more recently Crump and Seinfeld, 1981; Crump et al., 1983; Park et al., 2001). In these studies, the combined effects of sedimentation, Brownian and turbulent diffusion to the walls are taken into account. Crump and Seinfeld's result can be written:

$$\beta = \frac{2A_s(k_e D_B)^{1/2}}{\pi A_b H} + \frac{u_t}{H}\coth\left(\frac{\pi u_t}{4}(k_e D_B)^{1/2}\right). \tag{18}$$

The wall loss rate β is written as the sum of two terms, the first one giving diffusional losses to the vessel walls and the second one losses at the vessel bottom by sedimentation. Turbulence effects appear in this expression *via* the eddy diffusivity k_e which can be related to the Kolmogorov shear rate Γ using $k_e = K^2 \times \sqrt{2\Gamma/15}$, where $K = 0.4$ is the Karman constant (Corner and Pendlebury, 1951; Crump et al., 1983; Okuyama et al., 1986). To evaluate the relative importance of diffusion and sedimentation in the present study, the turbulent diffusion coefficient is approximated as $k_e x^y$, with $y = 2$ (x is the distance from the wall). The mean aerosol radius is used to calculate the particle Brownian diffusion coefficient D_B and terminal velocity u_t, H is the height of the tank reactor and A_s and A_b are the areas of its sidewall and bottom surface. Due to the relatively large particle size used in our study (the particle radius was always larger than 1 μm), it is found that losses due to sedimentation dominate. Typically, the wall loss due to diffusion is at least 20 times smaller than that due to sedimentation. Moreover, it is important to note that losses by sedimentation are not significantly influenced by turbulence because within the range of particle radii and Kolmogorov shear rates reached in our study, $\coth(\pi u_t \sqrt{k_e D}/4) \approx 1$, so that $\beta^- = u_t/H \approx \beta^+ = (u_t/H)\coth(\pi u_t \sqrt{k_e D}/4)$.

Once the grid is moving, it can collect particles by interception and inertial impaction, the dominant mechanisms for the particle size range used in this study (see for instance Hinds, 1999). However, the loss rates for these two mechanisms, which can be estimated by correlations used in filtration studies for single-fiber collection efficiency (Hinds, 1999), are much smaller that the one for differential sedimentation. Small droplet to grid rod size ratio and small particle Stokes number for the flow around the grid rods are responsible for the low efficiency of interception and inertial impaction respectively.

Consequently, we can assume that in our experimental conditions $\tau_l^-(a) \approx \tau_l^+(a) \approx u_t/H$ and that Eq. (15) is correctly approximated by Eq. (16). This assumption, partly based on engineering correlations, will be checked *a posteriori* using our experimental results. Indeed, they show that $\mathrm{d}(\langle a\rangle(t)/a_0)/\mathrm{d}t$ is proportionnal to n_i, which confirms that the term related to particle loss in Eq. (15) can be neglected.

4.2.2. Time domain validity for the $O(t)$ approximation

Eq. (16) is valid when order $O(t^2)$ terms are neglected. This can be quantified by comparing the coefficient $A(a)$ and $B(a)$ of Eq. (12), $B(a)$ being given by:

$$2B(a) = -\frac{A^*(a)}{\tau_l^+(a)} + n_i \int_0^a \frac{K(a',a'')}{2}\left(P(a')A^*(a'') + P(a'')A^*(a')\right)\frac{a^2\,\mathrm{d}a'}{\left(a^3 - a'^3\right)^{2/3}} - n_i \int_0^\infty K(a,a') \times \left(P(a)A^*(a') + P(a')A^*(a)\right)\mathrm{d}a'. \tag{19}$$

In order to get a rough estimate of the ratio $B(a)/A^*(a)$, we consider the case of a perfectly monodisperse distribution of radius a_0. Introducing $k = K(a_0, a_0)$, we find that neglecting $O(t^2)$ terms is valid when $t \ll \min(2H/ut, 2/kn_i)$. As in our experiments, measured values for the coalescence rate constant are in the range 1000–4000 $\mu m^3\,s^{-1}$, see next section, the previous condition on t reads $t \ll 500$ s.

5. Discussion of experimental results and comparison with theory

The temporal evolution of the mean aerosol radius $\langle a\rangle(t)$ was measured using the PDA technique presented in Section 2.3.2 and the initial aerosol number density n_i was measured with the light attenuation technique, see Section 2.3.3. A typical plot of $\langle a\rangle(t)/a_0$ as a function of time is shown in Fig. 4. For this particular set of experiments, the aerosol size distribution was measured for 10 min and the grid turned on after 3 min. The mean drop radius increases as soon as the grid is turned on and $\langle a\rangle/a_0$ is a linear function of time for a short time interval thereafter, as expected from Eq. (16). The slope b was obtained by fitting the data by a linear function in the time range when the linear behavior was observed (from $t = 180$ to $t = 280$ s for the curve shown in Fig. 4). The uncertainty in the slope b was typically found to be in the range of 10–20%. Table 3 gives the experimental conditions (aerosol initial radius, number density, etc.) for each of the experiments.

In the following discussion, we first present several theoretical expressions for the coalescence rate constant $K(a', a'')$. These are *ideal* coalescence rate constants, the derivation of which do not take into account hydrodynamic and colloidal interactions between colliding particles. They are subsequently used in Section 5.2,

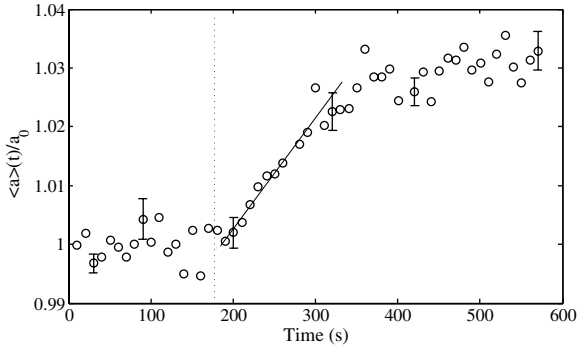

Fig. 4. A typical temporal evolution of $\langle a\rangle(t)/a_0$, as observed in our coalescence experiments. A linear increase of $\langle a\rangle(t)/a_0$ after initiation of the turbulent flow at $t = 180$ s is clearly displayed.

Table 3
Recap of experimental conditions for results shown in Figs. 5 and 6

Exp. number	a_0	σ_a/a_0	Number density ($\times 10^5$ particles cm^{-3})	$\langle\Gamma\rangle$ (s^{-1})	Pe
1	1.45 ± 0.03	0.16	10	88	22
2	1.1 ± 0.03	0.29	16	88	10
3	1.8 ± 0.05	0.16	8	88	42
4	1.95 ± 0.05	0.16	4	88	53
5	2.15 ± 0.06	0.2	3.5	88	71
6	1.24 ± 0.06	0.22	12	88	14
7	1.9 ± 0.03	0.17	6	88	49
8	1.44 ± 0.04	0.14	10	88	21
9	1.0 ± 0.03	0.24	20	88	7
10	2.5 ± 0.05	0.13	1.5	88	112
11	1.9 ± 0.02	0.17	5.4	59	34
12	1.7 ± 0.02	0.14	7.2	59	24
13	1.8 ± 0.06	0.14	5	59	27
14	1.1 ± 0.07	0.34	12	59	6
15	1.5 ± 0.04	0.15	11	59	16
16	2.4 ± 0.06	0.18	1.5	59	67
17	1.75 ± 0.06	0.11	3.2	25	11
18	1.1 ± 0.06	0.27	15.5	25	3
19	1.0 ± 0.04	0.19	26	25	2
20	1.05 ± 0.04	0.19	16	25	2
21	1.1 ± 0.02	0.24	16.5	25	3
22	1.3 ± 0.03	0.21	12.5	25	5
23	1.54 ± 0.05	0.15	10.7	25	7
24	1.95 ± 0.02	0.15	5.4	25	15
25	1.87 ± 0.04	0.16	5.4	25	13

Here, σ_a is the standard deviation of the best fitting gaussian distribution to the experimentally measured size distribution. The uncertainty on the spatially averaged Kolmogorov shear rate is given in Table 2. The Péclet number Pe is defined as $Pe = \langle\Gamma\rangle a_0^2/D_B$, where $D_B = k_b T/(6\pi\mu_f a_0)$ is the Brownian diffusivity coefficient (k_b is the Boltzmann constant, T the temperature and μ_f the gas viscosity).

where the experimental values for b/n_i are compared to theoretical predictions for the integral J defined in Eq. (16). The determination of J involves use of the experimentally measured initial drop size distribution in conjunction with a theoretical expression for the coalescence rate constant for drops of two sizes, i.e. $K(a', a'')$. In Section 5.3 we continue the discussion of the experimental results in the light of more recent theoretical results which take the hydrodynamic and colloidal interactions between colliding particles into account.

5.1. Ideal coalescence rate constants

The coalescence of drops in a turbulent flow is driven by four physical effects: the Brownian motion of the drops, their relative motion driven by the local shearing motion of the turbulence, the differences in their settling velocities, and their relative motion driven by turbulent accelerations.

The ideal rate for Brownian motion induced coalescence K_{br} is given by:

$$K_{\mathrm{br}}(a,a') = \frac{2k_{\mathrm{b}}T}{3\mu_{\mathrm{f}}}\left(\frac{1}{a}+\frac{1}{a'}\right)(a+a'), \tag{20}$$

where the Cunningham correction was taken to be one, which is justified for the particle size range considered in the present study. Saffman and Turner (1956) derived the rate constant for drops in turbulent shear flow that is persistent over the time period of the drops interaction and obtained:

$$K_{\mathrm{s}}(a,a') = \sqrt{\frac{8\pi}{15}}\,\Gamma(a+a')^3. \tag{21}$$

Consideration of the finite persistence time of turbulent shear leads to a small (approximately 15%) decrease in the rate constant (see Chun and Koch, 2005). When the Stokes number for the droplets is finite, their inertia can lead to a preferential concentration wherein the pair probability density for the drops in close proximity and the coalescence rate are enhanced. The Stokes number, which is defined as $St = \tau_{\mathrm{p}}/\tau_k$ where $\tau_{\mathrm{p}} = 2\rho_{\mathrm{p}}a^2/9\mu_{\mathrm{f}}$ is the particle viscous relaxation time and $\tau_k = 1/\langle\Gamma\rangle$ the Kolmogorov time scale, was always $\mathrm{O}(10^{-3})$ in our experiments. For the values of St and η/a in our experiments, the influence of preferential concentration on the coalescence rate constant is predicted to be only about 0.5% (Chun and Koch, 2005) and can be neglected. An ideal coalescence rate constant that accounts for gravity, turbulent shear and turbulent acceleration was derived by Saffman and Turner and slightly corrected by Wang et al. (1998):

$$K_t(a,a') = \sqrt{8\pi}(a+a')^2\left[\frac{1}{15}\Gamma^2(a+a')^2 + \left(1-\frac{\rho_{\mathrm{f}}}{\rho_{\mathrm{p}}}\right)^2\left\{\tau_{\mathrm{p}}(a')-\tau_p(a)\right\}^2\times\left(1.3g_k^2+\frac{\pi}{8}g^2\right)\right]^{1/2}, \tag{22}$$

where $g_k = \eta\Gamma^2$ is the turbulent acceleration experienced by aerosol droplets much smaller than the Kolmogorov length scale.[3] Turbulent acceleration and gravity induced coalescence are absent for drops of the same size so that $K_t(a,a) = K_{\mathrm{s}}(a,a)$.

A rough estimate for the relative importance of the various coalescence mechanisms taken into account in Eq. (22) can be obtained by using the ideal coalescence rate constants (which will be denoted as k^0) obtained from Eq. (22), when considering each coalescence mechanism acting separately. Thus, the ideal coalescence rate constant for turbulent shear induced coalescence is $k^0_{\mathrm{shear}} = K_t(a,a)$ and that for Brownian coalescence is $k^0_{\mathrm{br}} = K_{\mathrm{br}}(a,a)$. The ideal coalescence rate constant for turbulent acceleration induced coalescence, k^0_{acc}, is obtained by taking $g = 0$ in Eq. (22), discarding the turbulent shear induced contribution and considering $a' = a + \sigma_a$. Here, σ_a is the standard deviation of the Gaussian distribution that gives the best fit to the experimentally measured size distribution (see Table 3). One can obtain k^0_{sed} in a similar manner but setting $g_k = 0$ rather than $g = 0$. The ratios of the ideal rate constants obtained in this way are

$$\frac{k^0_{\mathrm{br}}}{k^0_{\mathrm{shear}}} = 0.26\frac{k_{\mathrm{b}}T}{\mu_{\mathrm{f}}\Gamma a^3},\quad \frac{k^0_{\mathrm{acc}}}{k^0_{\mathrm{shear}}} = 4.4St\frac{\eta}{a}\frac{\sigma_a}{a},\quad \frac{k^0_{\mathrm{sed}}}{k^0_{\mathrm{shear}}} = \frac{5\pi}{6}\frac{\sigma_a\rho_p g}{\mu_f\Gamma}\ \text{ and }\ \frac{k^0_{\mathrm{acc}}}{k^0_{\mathrm{sed}}} = 1.8\frac{g_k}{g}. \tag{23}$$

For the Kolmogorov shear rates and initial particle radii in our study, $k^0_{\mathrm{br}}/k^0_{\mathrm{shear}}$ is in the range 0.05–2, indicating that Brownian motion also plays a significant role in driving coalescence events (Okuyama et al., 1978). Making use of the measured standard deviations of the drop radius in our study, we find that the ideal rate due to turbulent shear is comparable to or slightly larger than that due to sedimentation, $k^0_{\mathrm{shear}}/k^0_{\mathrm{sed}} \approx \mathrm{O}(1)$. The turbulent accelerations experienced by the aerosol droplets are always smaller than acceleration due to gravity.

[3] Kruis and Kusters (1997) propose an additional term associated with spatial variations of the turbulent acceleration rate in their variant of Eq. (22), but this term is small when the particle radius is small compared with the Kolmogorov scale and the Stokes number is small. These conditions are satisfied in our study.

For the three Kolmogorov shear rates used in our study, $\langle \Gamma \rangle = 88$, 59, and 25 s^{-1}, the values of g_k are respectively 3.1, 1.7, and 0.5 $m^2\,s^{-1}$ and then the ratios k^0_{acc}/k^0_{sed} are 0.57, 0.31, and 0.085. This rough analysis suggests that the effects of polydispersity and differential sedimentation are important in our experiment, while turbulent acceleration is a secondary effect. However, it should be noted that the above estimates are based on ideal coalescence rate constants and the ratio of the actual coalescence rate constant to the ideal rate constant (namely the coalescence efficiency) can be much smaller than one (see discussion in Section 5.3).

5.2. Comparison of experimental results with predictions based on ideal coalescence rate constants

Fig. 5 is a plot of our results for b/n_i as well as the theoretical predictions for this ratio obtained by evaluating J using ideal collision rate constants based on the various coalescence mechanisms described in the preceding section. These results are plotted as a function of the Péclet number Pe defined as: $Pe = \langle \Gamma \rangle a_0^2/D_B$, where $D_B = k_b T/(6\pi\mu_f a_0)$ is the Brownian diffusivity coefficient (k_b is the Boltzmann constant, T the temperature and μ_f the gas viscosity). The error bars given for the theoretical predictions J result from the uncertainty in $\langle \Gamma \rangle$ and in the measurement of the initial size distribution. Our experimental results for b/n_i (black diamonds in Fig. 5) are found to be in good agreement with the theoretical predictions, denoted by squares in Fig. 5, that consider the coalescence rate constant to be a linear superposition of the ideal rate constants for turbulent shear (Eq. (21)) and Brownian motion (Eq. (20)). Theoretical predictions based on turbulent shear alone (circles on Fig. 5) underestimate the measured coalescence rates for $Pe < 10$. This could be expected based on the previous experiments of Okuyama et al. (1978), who found that Brownian coagulation cannot be ignored when $k^0_{br}/k^0_{shear} > 0.1$. The estimates of the ideal coalescence rate constants given above suggested that coalescence due to differential sedimentation also plays an important role in our experiments. A theoretical prediction (given by the diamonds in Fig. 5) that includes all of the driving forces (turbulent shear and acceleration, gravity, and Brownian motion) can be obtained by adding the rate constant (Eq. (22)) obtained from Saffman and Turner's second expression with that (Eq. (20)) for Brownian coalescence. It may then be surprising to see that this prediction significantly overestimates the experimentally measured rate of growth of the aerosol radius (the experimental results are on average 40% smaller than this prediction). However, this observation is consistent with the previous experimental studies of Okuyama et al. (1977), Okuyama et al. (1978) who found that their experimental measurements were close to the predictions obtained from superimposing shear and Brownian coalescence rates (i.e, using $K(a,a') = K_s(a,a') + K_{br}(a,a')$) whenever the drop radius and Kolmogorov shear rates were small enough so that $a_0^3\sqrt{\Gamma^2 v} < 2.5 \times 10^{-10}$ m s^{-1}. Our experimental conditions all lie within the range of conditions for which $a_0^3\sqrt{\Gamma^2 v} < 2.5 \times 10^{-10}$ m s^{-1} and $K_s(a_0,a_0) + K_{br}(a_0,a_0)$=1000 – 4000 $\mu m^3\,s^{-1}$.

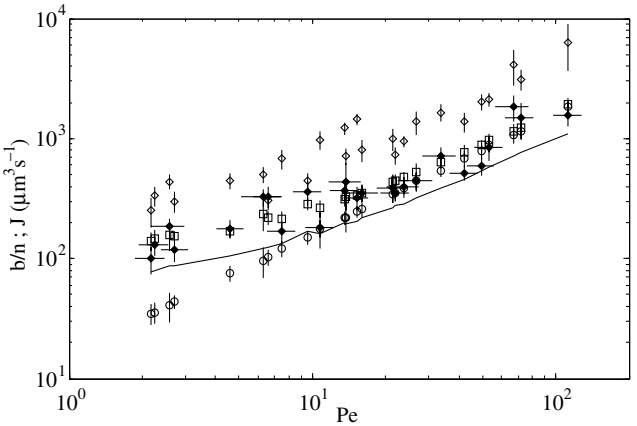

Fig. 5. Values of b/n_i (filled diamond) and J (unit: $\mu m^3\,s^{-1}$), plotted as a function of Pe. Several expressions were used for $K(a,a')$ in order to compute J: $K(a,a') = K_s(a,a') + K_{br}(a,a')$ (squares), $K(a,a') = K_s(a,a')$ (circles), $K(a,a') = K_t(a,a') + K_{br}(a,a')$ (diamonds) and $K(a,a') = k(a_0)$ given by Chun and Koch's monodisperse theory (solid line).

The analysis in this paper is predicated on the assumption that the variation in the mean droplet radius with time results from coalescence of drops rather than any other mechanism such as the deposition of drops on the walls or grid in the reactor, see Eq. (16). This assumption can be *a posteriori* validated by examining the dependence of the change in droplet size on the initial number density. If coalescence is responsible for the aerosol mean radius evolution, as predicted by Eq. (16), the rate of change of the aerosol mean radius with time (the slope b of the best fitting linear function of $\langle a\rangle(t)/a_0$ at short times) is equal to $n_i \times J$. In Fig. 6, we plotted b/J as a function of the initial aerosol number density n_i, taking $K(a,a') = K_s(a,a') + K_{br}(a,a')$ to compute J. The main conclusion to be drawn from this graph is that the scaled rate increases linearly with number density as expected if preferential deposition is negligible and the change in droplet radius is due to coalescence alone (a similar conclusion would be obtained using the theoretical result of Chun and Koch $k(a_0)$ for $K(a,a')$, when computing J). Systematic deviations from linearity would have been a sign that, in addition to coalescence, preferential deposition was occurring.

5.3. Discussion of experimental results in light of theories for collision efficiency

Thus far we have compared the experimental measurements only to theoretical predictions for the ideal coalescence rate constants, i.e. those that neglect the effects of hydrodynamic and colloidal interactions between the particles. To our knowledge the only study of the actual coalescence rates of aerosols in turbulent flows including particle interactions is Chun and Koch's (2005) investigation for initially monodisperse aerosols for which turbulent shear and Brownian motion drive particle collisions. The collision efficiency, defined as the ratio of the coalescence rate constant obtained with particle interactions to the ideal coalescence rate constant, was found to be ≈0.6, in a *Pe* number range similar to that of our experimental study. This value is significantly higher than that typically found for colloidal particles in turbulent liquids (0.1–0.3). The relatively close agreement of the experiments with the ideal coalescence rate for turbulent shear and Brownian motion is consistent with the theoretical prediction that the collision efficiency is closer to one for aerosols than for hydrosols. However, a closer comparison of the theoretical predictions of Chun and Koch (shown as a solid line in Fig. 5, and obtained using their result $k(a_0)$ for $K(a,a')$ to compute J) and the experiments (black diamonds in Fig. 5) indicates that the experiments lie systematically above the monodisperse theory, the predictions of which are on average 32% smaller than the experimental results.

The observation that our experimental results for the droplet growth rate is higher than the complete theoretical prediction including particle interactions for the rate of growth from shear and Brownian motion is not surprising. We already noted in Section 5.1 from an estimate based on ideal coalescence rate constants that differential sedimentation caused by the polydispersity of the drop radius distribution should play a significant

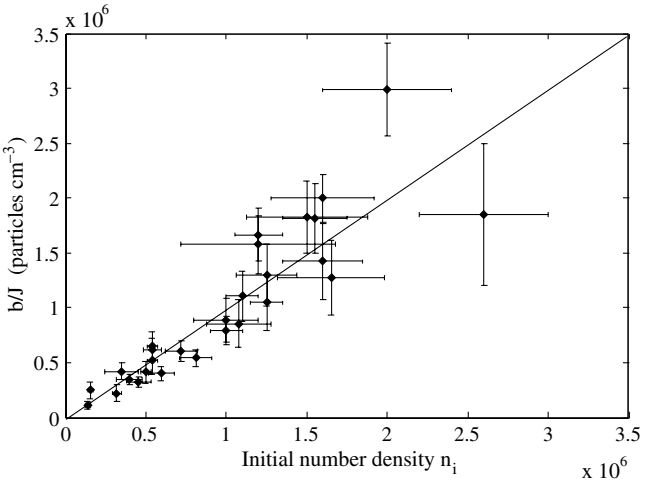

Fig. 6. Ratios b/J (unit: particles cm^{-3}) plotted as a function of the aerosol initial number density n_i. The values of J were computed with $K(a,a') = K_s(a,a') + K_{br}(a,a')$. The solid line is the first bisecting line and is given to highlight the linear variation of b/J with n_i.

role in determining the coalescence rate. Indeed, while the experiments were conducted with the most monodisperse aerosol that can be produced with current commercial technology at a number density sufficient to study coalescence, the degree of polydispersity is in fact high enough that the effects of turbulent acceleration and gravity on coalescence cannot be ignored (see Section 5.1 and Table 3). We have found that the difference between our experimental data and the theoretical predictions based on Chun and Koch's result is roughly proportional to $a_0^4(\sigma_a/a_0)$ and shows no systematic dependence on the turbulence intensity. This supports the fact that this difference may be due solely to a contribution from coalescence induced by differential sedimentation which, as has been shown in Section 5.1, is expected to dominate over turbulent acceleration induced coalescence. The mean difference between our experimental data points and Chun and Koch's predictions can then be minimized by assuming that an extra contribution of differential sedimentation induced coalescence, with a *constant* efficiency, is added to Chun and Koch's result. The value of the efficiency for gravity-driven coalescence thus found is 0.18. The mean of the absolute value of the difference between our experimental data points and this new theoretical prediction is then found to be 18%, with experimental data points lying on both sides of the theoretical curve. This difference is comparable to the uncertainty in our experimental results. Davis (1984) calculated the collision efficiency for differential sedimentation of aerosols in a quiescent gas and found them to lie in the range 0.01–0.3. Although Davis' study did not cover the precise parameter regime probed by our study and did not include the coupling between effects of gravity and turbulent shear, his calculation provides some basis for a rough estimate of the effects of differential sedimentation in our system. The fact that our inferred gravitational collision efficiency lies within the range of efficiencies predicted by Davis lends credence to the proposition that the difference between our experimental results and the theory of Chun and Koch for turbulent shear and Brownian coalescence can be attributed to an additional contribution resulting from differential sedimentation driven coalescence.

6. Conclusion

In this paper, we investigated the rate of aerosol coalescence in a well characterized turbulent flow, using measurements of the evolution of the mean aerosol radius upon initiation of the turbulent flow, along with measurements of the initial number density of the drops.

As mentioned in the Introduction, we are aware of only three previous studies that focused on turbulence-induced coalescence in aerosols. These studies measured the decay of the number density of a solid aerosol after a turbulent flow field was initiated. Taking proper account of the loss of particles due to wall deposition and sedimentation that also contributed to the number density decay, the coalescence rate constant was extracted from the data.

First, it should be mentioned that our experimental procedure is quite different from the one used in these studies. We worked with an oscillating grid generated turbulence chamber in a *continuous* mode of operation and measured the mean aerosol radius rather that the aerosol number density. Rapid changes of the mean aerosol radius $\langle a\rangle(t)$, after initiation of the turbulent flow, were measured using phase-Doppler anemometry and were related to the coalescence rate constant. Note that this approach is made possible by the good temporal and drop size resolution of phase-Doppler anemometry, which permits small variations of the mean drop radius, occurring over a short time scale, to be measured.

Second, the Kolmogorov shear rate, that is the shear rate of the small scales of the turbulent flow that are responsible for coalescence, was determined from measurements of the root-mean-square fluctuating velocity and the integral length scale of the turbulent flow. Langstroth and Gillepsie (1947) did not characterize the flow field in their turbulence chamber which renders any comparisons of their data with ours impossible. Okuyama et al. (1977) used a rotating stirrer to generate a turbulent flow field whereas in Okuyama et al. (1978), a turbulent pipe flow was considered. In both cases, engineering correlations were used to estimate the turbulent dissipation rate ϵ and the Kolmogorov shear rate $\Gamma = (\epsilon/\nu)^{1/2}$. In both studies, the mean solid aerosol radius was $a_s \approx 0.45$ μm (with geometric deviation in the range 1.2–1.5). As the Kolmogorov shear rates were large, $\Gamma = 400$–$40{,}000\ s^{-1}$, the Péclet numbers in these studies were in the same range as the ones obtained in our experiments (where larger particle sizes and smaller shear rates were used). A good match between our experimental results and theoretical predictions was obtained when considering a coalescence rate constant equal to that obtained by summing the ideal coalescence rate constants for turbulent shear and

Brownian motion, which is in agreement with the conclusions reached by Okuyama et al. (1977) and Okuyama et al. (1978).

However, linear superposition of ideal rate constants for each mechanism is not a reliable means of predicting actual coalescence rate constants, and comparisons based of such predictions with experiments may be misleading. Recent studies of aerosol coalescence and hydrosol coagulation indeed show that the coupling between the various mechanisms driving coalescence is not additive and, on the other hand, the overall collision efficiency is significantly lower than one (Brunk et al., 1998a; Chun and Koch, 2005). Our data lie systematically above the predictions of Chun and Koch regarding the coalescence rate constant of a monodisperse aerosol for which turbulent shear and Brownian motion drive particle collisions, with van der Waals and hydrodynamic interactions between colliding particles. Even if this discrepancy can be attributed to an additional contribution resulting from differential sedimentation driven coalescence, we think our results should rather be compared with a theory including all the driving mechanisms for coalescence as well as colloidal and hydrodynamic forces. We believe our results could be used to test such a theory which is, to our knowledge, not yet available.

Acknowledgement

Financial support for this work was provided by NASA grant NAG3-2349. Paul Duru thanks Sylvie Lorthois for her careful reading of the manuscript.

Appendix I. Mean oscillatory flows and turbulent velocity fluctuations

This appendix gives details about the processing of our LDV data, the results of which were presented in Section 3.1. Power spectra for horizontal and vertical velocity fluctuations measured by LDV displayed a frequency range where the spectrum decayed as $f^{-5/3}$, as expected from theoretical predictions for the spectral decay in the inertial subrange of turbulence. Peaks at the grid frequency ($f = 4$ Hz) and its harmonics appeared superimposed on the turbulence spectrum. These peaks were particularly prominent in the spectrum for the vertical velocity fluctuations in the grid region. The amplitude of the peaks decreased when z became equal to or larger than $B/2$. These spectra showed that, as may be expected, forced oscillatory flows are superimposed on turbulence, especially in the grid region. Determination of the turbulent kinetic energy required that we separated the velocity fluctuations u' resulting from turbulence from the velocity $\langle u\rangle$ of the forced oscillatory mean flow in order to establish the relative contribution that each of these flows makes to drop coalescence. The area under the velocity spectrum gives the mean-square velocity $\langle u^2\rangle = \langle u\rangle^2 + \langle u'^2\rangle$. Here, the angle brackets indicate an ensemble average, $u' = u - \langle u\rangle$, and u can refer to either u_x or u_z. The ensemble average velocity $\langle u\rangle$ is presumably an oscillatory function of time and its time average is nearly zero. Thus we assumed that the mean-square fluctuation, $\langle u'^2\rangle$, can be obtained as the area under a filtered spectrum. The filtered spectrum was obtained by replacing the value of the spectrum in the peaks at the forcing frequency and its harmonics by the mean of the surrounding values to obtain a smooth power spectrum. The square of the mean oscillatory velocity driven directly by the grid was then obtained as the difference between the areas under the original and filtered spectra. The autocorrelation functions for velocity fluctuations were obtained by taking the inverse Fourier transform of the filtered spectra.

The mean-square horizontal velocity is dominated by the turbulent fluctuations even within the grid region. For measurements throughout the region $0 < z < B/2 + 1$ cm, the ratio $\langle u_x\rangle/\langle u_x'^2\rangle^{1/2}$ was typically about 0.2, so that $\langle u_x^2\rangle \approx \langle u_x'^2\rangle$. In contrast, the mean flow made substantial contributions to $\langle u_z^2\rangle$. The values of $\langle u_z\rangle/\langle u_z'^2\rangle^{1/2}$ varied considerably as the position of the measuring volume was translated to different positions within a unit cell of the grid. On average, this ratio was approximately 0.66 within 0 cm $< z < B/2 + 1$ cm. The oscillatory mean flows are controlled by the grid geometry and a conservative estimate of the shearing produced by these structures is $\Gamma_{\text{mean}} \approx 2\langle u_z\rangle/M$ (M is the grid mesh spacing), which is much smaller than the estimated Kolmogorov shear rate (see Table 2). The root-mean-square of the velocity fluctuations, $\langle u_x'^2\rangle^{1/2}$ and $\langle u_z'^2\rangle^{1/2}$ are obtained from the filtered velocity spectra. In Section 3 of this paper, we refer to these values simply as u_x' and u_z'.

References

Abbott, C.E., 1974. Experimental cloud droplet collection efficiencies. J. Geophys. Res. 79, 3100–3998.

Brumley, B.H., Jirka, G.H., 1987. Near-surface turbulence in a grid-stirred tank. J. Fluid Mech. 183, 235–263.

Brunk, B.K., Koch, D.L., Lion, L.W., 1998a. Turbulent coagulation of colloidal particles. J. Fluid Mech. 364, 81–113.

Brunk, B.K., Koch, D.L., Lion, L.W., 1998b. Observations of coagulation in isotropic turbulence. J. Fluid Mech. 371, 81–107.

Chun, J., Koch, D.L., 2005. Coagulation of monodisperse aerosol particles by isotropic turbulence. Phys. Fluids 17 (2), art. No. 027102.

Chun, J., Koch, D.L., Rani, S.L., Ahluwalia, A., Collins, L.R., 2004. Clustering of aerosol particles in isotropic turbulence. J. Fluid Mech. 536, 219–251.

Corner, J., Pendlebury, E.D., 1951. The coagulation and deposition of a stirred aerosol. Proc. Phys. Soc. B 64, 645–654.

Crowe, C., Sommerfeld, M., Tsuji, Y., 1998. Multiphase Flows with Droplets and Particles. CRC Press.

Crump, J.G., Seinfeld, J.H., 1981. Turbulent deposition and gravitational sedimentation of an aerosol in a vessel of arbitrary shape. J. Aerosol Sci. 12, 405–415.

Crump, J.G., Flagan, R.C., Seinfeld, J.H., 1983. Particle wall loss rates in vessels. Aerosol Sci. Technol. 2, 303–309.

Davis, R.H., 1984. The rate of coagulation of a dilute polydispersed system of sedimenting spheres. J. Fluid Mech. 145, 179–199.

De Silva, I.P.D., Fernando, H.J.S., 1992. Some aspects of mixing in a stratified turbulent patch. J. Fluid Mech. 240, 601–625.

E, X., Hopfinger, E.J., 1986. On mixing across an interface in stable stratified fluid. J. Fluid Mech. 166, 227–244.

Edwards, R.V., 1987. Report of the special panel on statistical particle bias problems in laser anemometry. J. Fluids Eng. 109, 89–93.

Edwards, C.F., Marx, K.D., 1992. Analysis of the ideal phase-Doppler system: limitations imposed by the single-particle constraint. Atomization and Sprays 2, 319–366.

Findheisen, W., 1939. Zur Frage der Regentröpfenbildung in reinem Wasserwolken. Meteor. Z. 56, 365–368.

Friedlander, S.K., 2000. Smoke, dust, and haze, second ed.. In: Fundamentals of aerosols dynamics Oxford University Press.

Hannoun, I.A., Fernando, H.J.S., List, E.J., 1988. Turbulence structure near a sharp density interface. J. Fluid Mech. 18, 189–209.

Hinds, W.C., 1999. Aerosol technology. Properties, behavior and measurement of airbone particles, second ed.. In: Fundamentals of aerosols dynamics Wiley-Interscience.

Hopfinger, E.J., Toly, J.-A., 1976. Spatially decaying turbulence and its relation to mixing across density interfaces. J. Fluid Mech. 78, 155–175.

Krone, R.B., 1978. In: Kjerfve, B. (Ed.), Estuarine Transport Processes: Symposium. University of South California Press.

Kruis, F.E., Kusters, K.A., 1997. The collision rate of particles in turbulent flow. Chem. Eng. Commun. 158, 201–230.

Langstroth, G.O., Gillepsie, T., 1947. Coagulation and surface losses in disperse systems in still and turbulent air. Canad. J. Res. B 25, 455–471.

Okuyama, K., Kousaka, Y., Kida, Y., Yoshida, T., 1977. Turbulent coagulation of aerosols in a stirred tank. J. Chem. Eng. Jpn. 10 (2), 142–147.

Okuyama, K., Kousaka, Y., Yoshida, T., 1978. Turbulent coagulation of aerosols in a pipe flow. J. Aerosol Sci. 9, 399–410.

Okuyama, K., Kousaka, Y., Yamamoto, S., Hosokawa, T., 1986. Particle loss of aerosols with particle diameters between 6 and 2000 nm in stirred tank. J. Colloid Interface Sci. 110 (1), 214–223.

O'Melia, C.R., 1980. Aquasols: the behavior of small particles in aquatic systems. Environ. Sci. Technol. 14, 1052–1060.

Park, S.H., Kim, H.P., Han, Y.T., Kwon, S.B., Lee, K.W., 2001. Wall loss rate of polydispersed aerosols. Aerosol Sci. Technol. 35, 710–717.

Reade, W.C., Collins, L.R., 2000. Effect of preferential concentration on turbulent collision rates. Phys. Fluids 12, 2530–2540.

Saffman, P.G., Turner, J.S., 1956. On the collision of drops in turbulent clouds. J. Fluid Mech. 1, 16–30.

Shaw, R.A., 2003. Particle–turbulence interactions in atmospheric clouds. Annu. Rev. Fluid Mech. 35, 183–227.

Sundaram, S., Collins, L.R., 1997. Collision statistics in an isotropic particle-laden turbulent suspensions. Part 1. Direct numerical simulations. J. Fluid Mech. 335, 75–109.

Tennekes, H., Lumley, J.L., 1972. A First Course in Turbulence. MIT Press.

Thompson, S.M., Turner, J.S., 1975. Mixing across an interface due to turbulence. J. Fluid Mech. 67, 349–368.

Townsend, A.A., 1976. The Structure of Turbulent Shear Flow, second ed. Cambridge University Press.

van de Hulst, H.C., 1981. Light Scattering by Small Particles. Dover Publications.

von Smoluchowski, M., 1916. Drei Vorträge über Diffusion, brownsche Bewegung und Koagulation von Kolloidteilchen. Phys. Z. 17, 557–585.

von Smoluchowski, M., 1917. Versuch einer mathematischen Theorie der Koagulationskinetik kolloider Lösungen. Z. Phys. Chem. 92, 129–168.

Wagner, P.E., Kerker, M., 1977. Brownian coagulation of aerosols in rarefied gases. J. Chem. Phys. 66, 638–646.

Wang, L.-P., Wexler, A.S., Zhou, Y., 1998. Statistical mechanical descriptions of turbulent coagulation. Phys. Fluids 10 (10), 2647–2651.

Wang, L.-P., Wexler, A.S., Zhou, Y., 2000. Statistical mechanical description and modelling of turbulent collision of inertial particles. J. Fluid Mech. 415, 117–153.